ACS APPLIED ENERGY MATERIALS

www.acsaem.org Article

Electrochemical Properties of a La-Doped $Na_5YSi_4O_{12}$ Ceramic Electrolyte

Mohamed M. Abdelaal, Zhongting Wang, Hailin Shen,* Zhenghui Pan,* and Masashi Kotobuki*

Cite This: ACS Appl. Energy Mater. 2025, 8, 9656−9662 Read Online

ACCESS | Metrics & More | Article Recommendations | Supporting Information

ABSTRACT: Solid-state sodium batteries operating at ambient temperatures are promising alternatives to liquid electrolyte batteries, offering improved safety and higher energy density. Among solid-state electrolytes, the ceramic Na-conducting electrolyte $Na_5YSi_4O_{12}$ (N5) stands out due to its high Na-ion conductivity, wide electrochemical stability window, and compatibility with high-energy-density cathodes. However, achieving high ionic conductivity at room temperature remains a challenge. In this study, the effect of La doping on the electrochemical properties of an N5 ceramic electrolyte is systematically investigated. By optimizing the molar ratio of La_2O_3, La is successfully doped at the Y-site, leading to lattice parameter expansion, as confirmed by Rietveld refinement of the XRD data. Scanning electron microscopy analysis reveals significant changes in grain boundary morphology in La-doped $Na_5YSi_4O_{12}$, resulting in an increase in grain boundary ionic conductivity from 1.6×10^{-4} S cm^{-1} of the pristine one to 4.3×10^{-4} S cm^{-1}. Additionally, La doping preserves the low activation energy (0.19 eV) and high electrochemical stability window (up to 8 V vs Na/Na^+). La-doped N5 demonstrates superior cycling stability for Na deposition/stripping, maintaining performance for over 1000 h at 15 μA cm^{-2}, compared to only 118 h for the pristine one. This study indicates that La-doped N5 is a promising solid electrolyte for all-solid-state Na batteries.

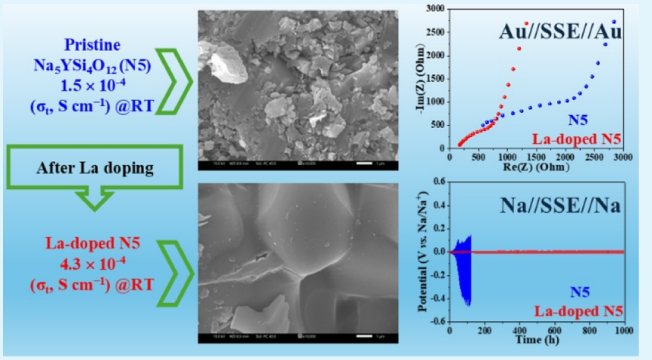

KEYWORDS: *rare-earth silicates, lanthanum doping, solid-state reaction, sintering aid, sodium batteries*

Downloaded via MING CHI UNIV TECH on September 5, 2025 at 07:13:03 (UTC).
See https://pubs.acs.org/sharingguidelines for options on how to legitimately share published articles.

1. INTRODUCTION

Sodium batteries are considered emergency devices instead of lithium batteries due to the abundance of sodium using similar mechanisms and techniques.[1−3] High energy density can be achieved if sodium metal is used as an anode in sodium metal batteries (SSBs) due to its high delivery capacity of ∼1166 mA h g^{-1} and low discharge potential.[4,5] However, dendrite formation and electrolyte leakage have caused safety issues.[6,7] Therefore, liquid electrolytes can be replaced by solid-state electrolytes (SSEs) to improve the battery safety and achieve higher energy density.[8]

Sodium rare-earth silicates have the formula $Na_5RSi_4O_{12}$ (N5), where *R* is a rare-earth element and feature nearly planar silicate rings linked by RO_6 octahedra, which can provide 3D ion conduction pathways, making it a promising SSE.[9] N5 can transform into less conductive secondary phases, such as $Na_9YSi_6O_{18}$ (N9) and $Na_3YSi_3O_9$ (N3).[10] These metastable phases possess more constrained structural frameworks. N9 is built from 12-membered silicate rings, within which Na^+ ions occupy annular cavities with limited interconnectivity, resulting in discontinuous ion migration pathways and restricted mobility.[11] Similarly, N3 features a compact arrangement of silicate tetrahedra and isolated sodium sites due to its lower sodium and yttrium content. This lack of extended pathways in N3 further inhibits the Na^+ transport. In both N3 and N9, the local electrostatic environment leads to strong binding of sodium ions, increasing activation energies for ion hopping and severely limiting ionic conductivity.[10]

N3 and N9 are metastable intermediates typically formed at lower processing temperatures or under off-stoichiometric conditions.[11,12] Du et al. demonstrated that sintering at 1150 °C for 36 h after calcining at 950 °C for 8 h yields a high-purity N5 phase, while deviations in temperature or dwell time resulted in the formation of mixed phases.[13]

Additives are widely used in solid-state reactions to improve synthesis conditions.[5,14] For example, P_2O_5 was utilized as a glass-forming oxide for interface engineering throughout introduction glassy phase between grains.[5] Although the glass phase would decrease the total ionic conductivity because it

Received: May 1, 2025
Revised: June 18, 2025
Accepted: June 23, 2025
Published: June 26, 2025

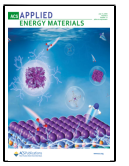

ACS Publications © 2025 American Chemical Society

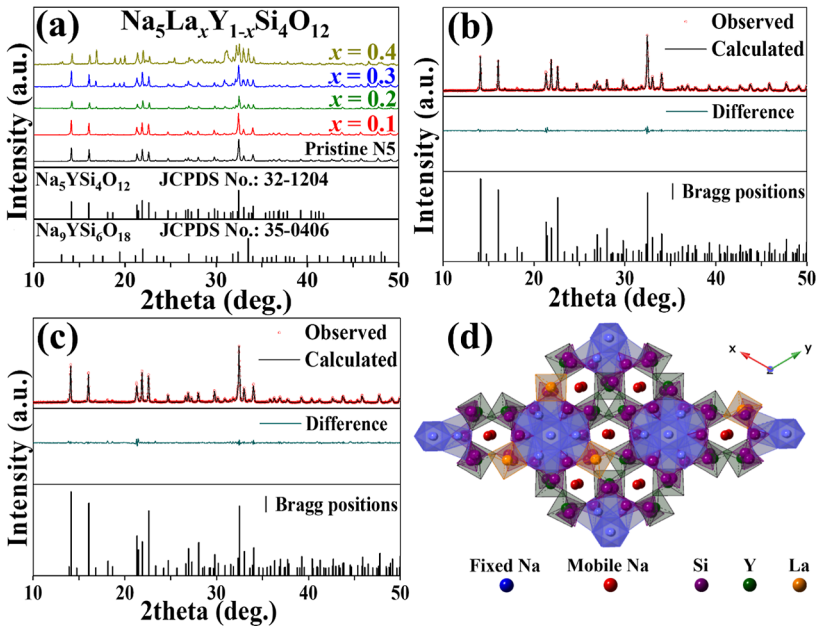

Figure 1. (a) XRD patterns of $Na_5La_xY_{1-x}Si_4O_{12}$ for x = 0.1−0.4; Rietveld refinement of XRD patterns for (b) $Na_5YSi_4O_{12}$ and (c) $Na_5La_{0.1}Y_{0.9}Si_4O_{12}$; and (d) schematic diagram of the crystal structure of $Na_5La_{0.1}Y_{0.9}Si_4O_{12}$.

decreased the crystalline content of N5, it exhibited very low initial interface resistance with metallic sodium.[5] Generally, additives could be used in the solid-state method for lowering reaction temperature,[15] improving ionic conductivity,[15] grain boundary modification,[16] phase stabilization,[5] enhancing mechanical properties,[17] and reducing dendrite growth.[18]

Lanthanum dioxide (La_2O_3) was used as a sintering additive in the $Li_2O-B_2O_3-SiO_2$ system.[15] Xia et al. reported that La_2O_3 breaks Si−O−Si bonds to create Si−O−La chemical bonds, increasing the mechanical strength.[19] Furthermore, La^{3+} ions can act as a dopant.[20] The ionic radius of La^{3+} (1.06 Å)[21] is close to Y^{3+} (0.9 Å),[22] making it a good candidate as a dopant of N5. To the best of our knowledge, La-doped N5 has never been investigated.

In this work, La_2O_3 was used for dual purposes as a sintering aid and dopant in the Y site in N5. Sinterability of the N5 pellet was improved by La_2O_3 addition, leading to higher ionic conductivity. Additionally, the La-doped N5 provided stable Na stripping/deposition behavior compared with pristine N5.

2. EXPERIMENTAL SECTION

2.1. Synthesis of La-Doped N5. All chemicals were used as received without further purification and handled inside an argon-filled glovebox to minimize exposure to moisture and CO_2. The precursors for $Na_5La_xY_{1-x}Si_4O_{12}$ (x = 0.0, 0.1, 0.2, 0.3, and 0.4), sodium carbonate anhydrous (Na_2CO_3, 99.5%, J.T.Baker), yttrium oxide (Y_2O_3, 99.9%, Sigma-Aldrich), silicon dioxide (SiO_2, 99.9%, Thermo Scientific Chemicals), and lanthanum oxide (La_2O_3, 99.9%, Sigma-Aldrich) were mixed in precise stoichiometric ratios using a pot-mill at 300 rpm for 24 h using 99.8% ethanol as the milling medium and a ball-to-powder volume ratio of 5:1. The milled powders were dried at 80 °C for 24 h and then calcined in an alumina crucible at 900 °C for 8 h in air, with a heating rate of 5 °C min^{-1}. The calcined powders were milled at 300 rpm for 2 h using 99.8% ethanol and a 5:1 ball-to-powder ratio. The resulting powders were pressed into pellets at 10 MPa. The pellets were then sintered in an alumina boat at 1100 °C for 36 h in air, at a heating rate of 5 °C min^{-1}. Grinding, calcination, and sintering were performed outside the glovebox under ambient conditions, while the final products were stored back inside the glovebox.

2.2. Material Characterizations. The crystalline structure of the materials was characterized by using X-ray powder diffraction (XRD, Bruker D2 PHASER, Bruker AXS Inc.). The XRD measurements were conducted using Cu Kα at 30 kV and 10 mA over a 2θ from 10° to 50°. To further refine the structural analysis, Rietveld refinement was carried out using TOPAS 4.2 software. The morphology and elemental distribution were investigated using a scanning electron microscope (SEM, JSM-IT200, JEOL Ltd., Tokyo, Japan) with EDS. The relative density of the as-synthesized pellets was determined using the Archimedean principle in n-butanol as an immersion medium, with a PRECISA XS 225A-SCS electronic balance and density measurement kits. Samples were immersed for 24 h at room temperature to ensure complete wetting and reliable density measurements.

2.3. Electrochemical Experiments. All cells used for electrochemical characterizations were assembled under an inert gas atmosphere inside a glovebox. Electrochemical measurements were carried out at room temperature, except for the Arrhenius plot analysis, where the cell temperature was stabilized for 1 h at each temperature before performing electrochemical impedance spectroscopy (EIS) measurements. A BioLogic SP-150e potentiostat/galvanostat was used for EIS, electronic conductivity measurements, and linear sweep voltammetry (LSV), while sodium plating and stripping experiments were performed using a NEWARE galvanic charger. Ionic conductivity and activation energy were measured on gold-sputtered pellets using EIS in a frequency range of 1 MHz ∼100 mHz with a sinusoidal voltage amplitude of 10 mV. The EIS spectra were analyzed using ZFit software integrated with the BioLogic software, and the ionic conductivity (σ) was calculated using eq 1.[23]

$$\sigma = \frac{l}{RA} \tag{1}$$

where l is the pellet thickness, R is the real part of the measured impedance, and A is the area of the blocking electrode. Activation energies were estimated from the Arrhenius plot based on eq 2.[13,24]

$$\sigma = A\exp(-E_a/k_BT) \tag{2}$$

wherein A is the Arrhenius pre-exponential factor, E_a is the activation energy, the Boltzmann constant (8.617×10^{-5} eV K^{-1}), and T represents the absolute temperature. Activation energy for bulk ionic conduction (σ_b) was estimated from the modified Arrhenius plot based on eq 3.[25]

https://doi.org/10.1021/acsaem.5c01301
ACS Appl. Energy Mater. 2025, 8, 9656−9662

$$\sigma_b T = A\exp(-E_a/k_B T) \quad (3)$$

Electronic conductivity (γ) was determined between two blocking electrodes using eq 4.[26,27]

$$\gamma = \frac{i_r l}{VA} \quad (4)$$

where i_r represents the residual current after 16 h and V is the applied voltage (1 V). The ionic transference number (t_i) was calculated using eq 5.[28]

$$t_i = \frac{\sigma_{ion}}{\text{total conductivity}} \quad (5)$$

where total conductivity is the sum of ionic and electronic conductivities.

LSV was conducted to evaluate the electrochemical stability window of SSE. The test was performed using a Na//SSE//stainless steel cell configuration, beginning at the open circuit potential and sweeping to 8 V vs Na/Na^+ at a scan rate of 0.1 mV s^{-1}.

Critical current density (CCD) was evaluated by incrementally applying current densities from 0.005 mA cm^{-2} to 0.50 mA cm^{-2}, with each step maintained for 30 min. The current was increased by 10 μA up to 0.2 mA cm^{-2}, after which it was increased by 100 μA. Long-term DC cycling was conducted at a constant current density of 15 μA cm^{-2}, with a step duration of 30 min.

3. RESULTS AND DISCUSSION

3.1. Solid Electrolyte Characterizations. The crystalline structure of the as-synthesized materials is exhibited in Figure 1a, with reference to standard diffraction patterns ($Na_5YSi_4O_{12}$, N5, JCPDS# 32-1204 and $Na_9YSi_6O_{18}$, N9, JCPDS# 35-0406) for comparison.[29] N5 was successfully synthesized without La_2O_3 addition. Only $Na_5La_{0.1}Y_{0.9}Si_4O_{12}$ was closely matched with a standard N5 reference pattern among the doped samples, while for higher doping ratios (x = 0.2, 0.3, and 0.4), additional phases such as N9 at 2θ of 33.5° and other impurities appeared, as shown in Figure S1. These impurities were identified as lanthanum silicate oxide (JCPDS# 76-0338), sodium silicate (JCPDS# 32-1154), and yttrium silicate (JCPDS# 21-1456).[30,31] The N9 structure, with its 12-membered silicate rings and annular cavities, offers a more flexible framework that can better accommodate larger rare-earth ions like La^{3+} compared to the more rigid N5 structure.[11]

Given that only $Na_5La_{0.1}Y_{0.9}Si_4O_{12}$ matched the pure N5 structure, this composition (La-0.1-N5), along with pristine N5, was selected for further investigation. Rietveld refinement of pristine N5 and La-0.1-N5 was performed as presented in Figure 1b and c, respectively. The lattice parameters ($a = b$, c) and unit cell volume (V) for the standard material, N5 and La-0.1-N5, are presented in Table S1. The lattice parameter a of N5 (21.818 Å) is slightly smaller than the standard (22.030), while the c-parameter (12.801 Å) is larger than the standard (12.620 Å).[13] This means there is some distortion in the crystal lattice of N5, possibly due to a prolonged sintering time.

The unit cell volume for N5 (5277 $Å^3$) is smaller than the standard value (5304.19 $Å^3$), indicating a denser packing of the structure due to synthesis conditions or stoichiometry.[13,32] For La-0.1-N5, the a-parameter increased to 22.766 Å, while the c-parameter decreased to 12.158 Å. Moreover, the cell volume expanded to 5457.2 $Å^3$, indicating that La doping in the Y site has significantly influenced the lattice dimensions.[32] This is likely due to doping of the larger ionic radius of La^{3+} (1.06 Å) in Y^{3+} (0.9 Å), which could change the unit cell dimensions.[21,22] Moreover, the occupancies of the La and Y sites were consistent with the expected stoichiometry (Table S2). Figure 1d presents a schematic diagram of the crystal structure of $Na_5La_{0.1}Y_{0.9}Si_4O_{12}$. The structure consists of a three-dimensional network formed by corner-sharing SiO_4 tetrahedra (shown in purple) that creates nearly planar silicate rings, which are interconnected through RO_6 octahedra (R = Y/La, shown in green/orange).[9] The La^{3+} ions (orange spheres) partially replace the Y^{3+} ions (green spheres) in the octahedral sites. The larger ionic radius of La^{3+} (1.06 Å) compared to that of Y^{3+} (0.900 Å) introduces local lattice distortion around the substitution sites.

The cross-sectional morphologies of N5 and La-0.1-N5 were investigated by SEM as shown in Figure 2. The grain

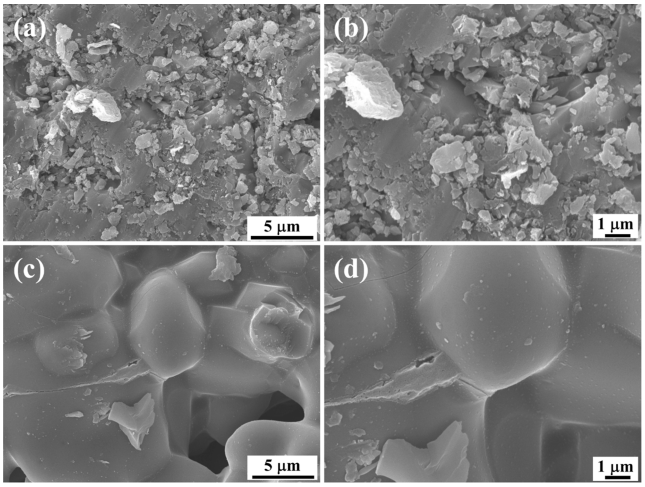

Figure 2. SEM images of (a,b) $Na_5YSi_4O_{12}$ and (c,d) $Na_5La_{0.1}Y_{0.9}Si_4O_{12}$.

boundaries of pristine N5 are irregular, less defined, and loosely connected with many small particles and fragments filling the gaps as shown in Figure 2a,b. In contrast, the doped one possesses more tightly packed and smoother grain boundaries, as shown in Figure 2c,d. Moreover, the surface texture of La-0.1-N5 was smoother and more compact than pristine N5. This indicates that La_2O_3 acted as a sintering aid. The measured relative densities of pristine N5 and La-0.1-N5 were 90.7% and 97.1%, respectively. The significant increase in relative density indicates that La_2O_3 has greatly enhanced the densification process, matching SEM images.[33,34]

As the La content increased from x = 0.2 to 0.4, the SEM cross-sectional images in Figure S2(a–f) reveal significant changes in the microstructure. At lower La concentrations (x = 0.2, Figure S2a,b), the grain boundaries were still distinct. With increasing La content to x = 0.3 and 0.4, the boundaries were unclear. This evolution in the microstructure indicates that La doping promoted the sintering of N5. However, an excessive La content led to the formation of secondary phases and abnormal grain growth.

The EDX detected only Na, Y, Si, and O elements in the pristine N5 sample, without other impurities as shown in Figure S3. For La-0.1-N5, La was observed in addition to Na, Y, Si, and O, confirming successful La doping in N5 as presented in Figure 3. The relative atomic ratio of pristine N5 elements is 21.3%, 4.1%, 20.9%, and 53.3% for Na, Y, Si, and O elements, respectively, as presented in Figure S4. The elemental proportions aligned well with the expected stoichiometry of the N5 compound.[35] Similarly, the atomic

https://doi.org/10.1021/acsaem.5c01301
ACS Appl. Energy Mater. 2025, 8, 9656−9662

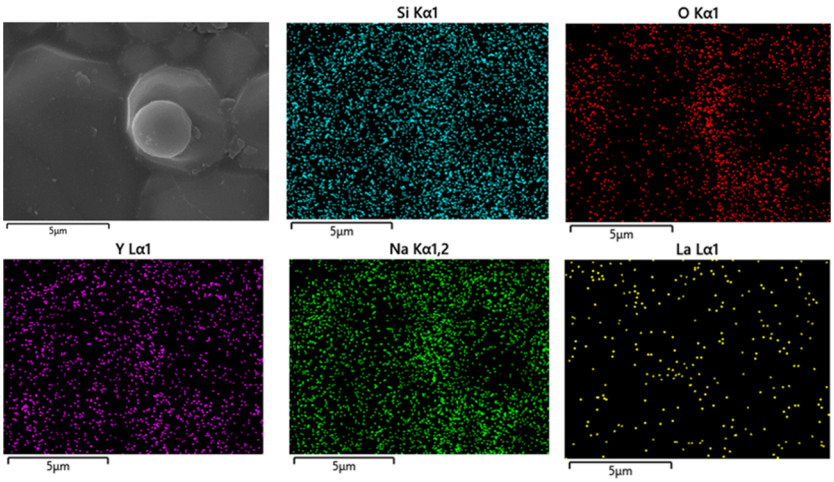

Figure 3. Elemental distribution of $Na_5La_{0.1}Y_{0.9}Si_4O_{12}$.

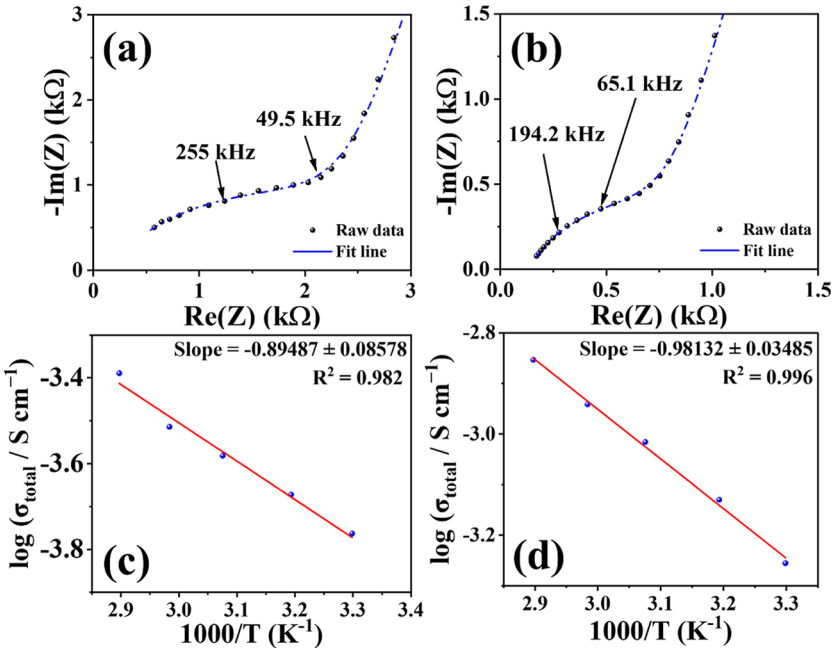

Figure 4. EIS measurements of (a) $Na_5YSi_4O_{12}$ and (b) $Na_5La_{0.1}Y_{0.9}Si_4O_{12}$ measured at room temperature, along with Arrhenius plots (c,d).

percentage of La-0.1-N5 proved that the expected chemical composition was obtained, as shown in Figure S5.

3.2. Electrochemical Performance. EIS for pristine N5 and La-0.1-N5 are shown in Figure S6a,b, respectively. The corresponding semicircles that appeared at high frequency are magnified in Figure 4a,b, respectively. Both showed an incipient semicircle at high frequency, followed by a tail at the midfrequency to the low frequency. The spectra were fitted by equivalent circuit model as presented in Figure S6c.[13,36,37] The bulk resistance was presented by (R_b), while the grain boundary impedance was presented by a time constant (Q_{gb} and R_{gb}).[32] Moreover, the charge polarization on the surface of the blocking electrode was presented by Q_c.[13]

The bulk ionic conductivity of pristine N5 and La-0.1-N5 was 2.5×10^{-3} S cm^{-1} and 2.4×10^{-3} S cm^{-1}, respectively, which implies the change in lattice parameters and volume cell due to La doping did not affect the ion migration in the crystal grains.[5] In contrast, the grain boundary conductivities of N5 and La-0.1-N5 were 1.6×10^{-4} S cm^{-1} and 5.3×10^{-4} S cm^{-1}. This significant increase is related to relative density and grain boundaries morphology.[29,35] As discussed in the SEM image, grain boundaries of La-0.1-N5 were more fused together with fewer irregularities. In addition, the grain shape became more rounded and had smoother edges, facilitating sodium-ion transport. The total ionic conductivity of La-0.1-N5 was 4.3×10^{-4} S cm^{-1}, which was higher than pristine N5 (1.5×10^{-4} S cm^{-1}).

As seen in Figure 4c,d, the activation energy of both materials was estimated to 0.18 eV vs 0.19 for pristine N5 and La-0.1-N5, respectively. The activation energies of bulk and grain boundaries are also analyzed in Figure S7(a–d) and Tables S3,S4. For the La-doped sample, the bulk activation energy remained unchanged at 0.14 eV, indicating that the Na^+ ion transport mechanism in the crystal lattice was preserved. Sodium-ion conduction in N5 primarily occurs along pathways formed by the nearly planar silicate rings linked via RO_6 (R = rare-earth element) octahedra.[35,38] Recent studies suggest that sodium-ion migration in N5-type materials is energetically

https://doi.org/10.1021/acsaem.5c01301
ACS Appl. Energy Mater. 2025, 8, 9656−9662

favorable along these channels.[11,20] Contrary, the grain boundary activation energy increased from 0.18 eV (pristine) to 0.22 eV (La-doped), possibly due to minor structural or chemical modifications at the grain boundaries induced by the La doping. Substituting Y with La could induce local lattice distortions or strain, particularly at grain boundaries, leading to an increase in the activation energy at the grain boundaries.

The electronic conductivity measurements of pristine N5 and La-0.1-N5 are shown in Figure 5a and b, respectively. The

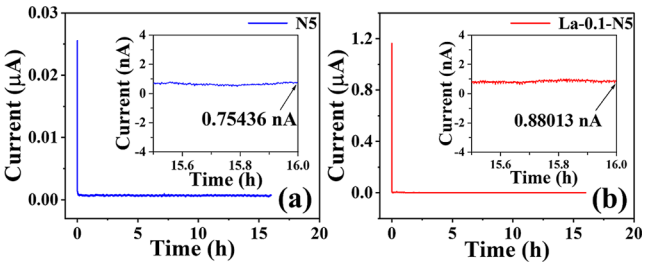

Figure 5. Electronic conductivity measurements of (a) $Na_5YSi_4O_{12}$ and (b) $Na_5La_{0.1}Y_{0.9}Si_4O_{12}$. Inset: magnified view of the final 0.5 h of the measurements.

electronic conductivity was calculated to be 4.1×10^{-11} S cm^{-1} and 5.1×10^{-11} S cm^{-1} for N5 and La-0.1-N5, respectively. This similarity in electronic conductivity means La doping did not affect the electrons movement. This means also the electrolyte mainly conducts ions while electrons do not easily flow.[39,40] Ionic transference number (t_i) was calculated to be 0.99 for both materials as presented in Table S5, which confirms that sodium ions are dominant conducting species.[28,39]

The linear sweep voltammetry (LSV) was used to measure the oxidative stability of pristine N5 and La-0.1-N5 as presented in Figure 6a. Both samples exhibited a superior electrochemical stability window until 8 V vs Na/Na^+ with the perspective to be coupled with high-voltage cathodes for high-energy density batteries.[38,40] This also means that a change in crystal structure and grain boundaries of the N5 structure due to La doping did not affect oxidation stability. Galvanic plating and stripping tests were performed to investigate compatibility with the Na metal anode. The reversible process of sodium plating and stripping implied the ability of SSEs to suppress dendrite formation during cycling.[5,27] Appling stepwise current densities showed that the CCD of La-0.1-N5 was 85 μA cm^{-2} (42.64 μA), while the CCD of pristine N5 was 300 μA cm^{-2} (150.6 μA) as shown in Figures 6b and S8a, respectively. Moreover, N5 exhibited lower polarization as compared to La-0.1-N5 at 5 μA cm^{-2}, as shown in Figure S8b.

To investigate the observed differences, EIS was performed on fresh cells, as presented in Figure 6c. The charge transfer resistance of La-doped N5 was significantly higher than that of N5. The compatibility between sodium metal and the samples (N5 and La-0.1-N5) was assessed by pouring molten sodium onto their surfaces, as presented in Figure S9. The pristine N5 exhibited better compatibility with sodium metal compared to La-0.1-N5, leading to lower interfacial resistance.[40,41] This higher interfacial resistance in La-0.1-N5 could explain its lower CCD, as it impedes fast charge transfer during high-current operation. This behavior may be attributed to La-doped N5 being more sodium-phobic than pristine N5.

A long-term DC cycling test at 15 μA cm^{-2} was performed to study sodium plating and stripping at fixed current as shown in Figure 6d. La-0.1-N5 showed superior stability during cycling, reaching more than 1000 h, while the pristine N5 made an internal short-circuit due to sodium dendrite formation after 118 h. The inset Figure 6d shows potential response over time for symmetric sodium cells using pristine N5 (blue) and La-0.1-N5 (red) at 15 μA cm^{-2}, which clearly indicated periodic plating and stripping of sodium in both samples. Initially, N5 exhibited lower voltage oscillations in the initial few hours compared to La-0.1-N5, and then the

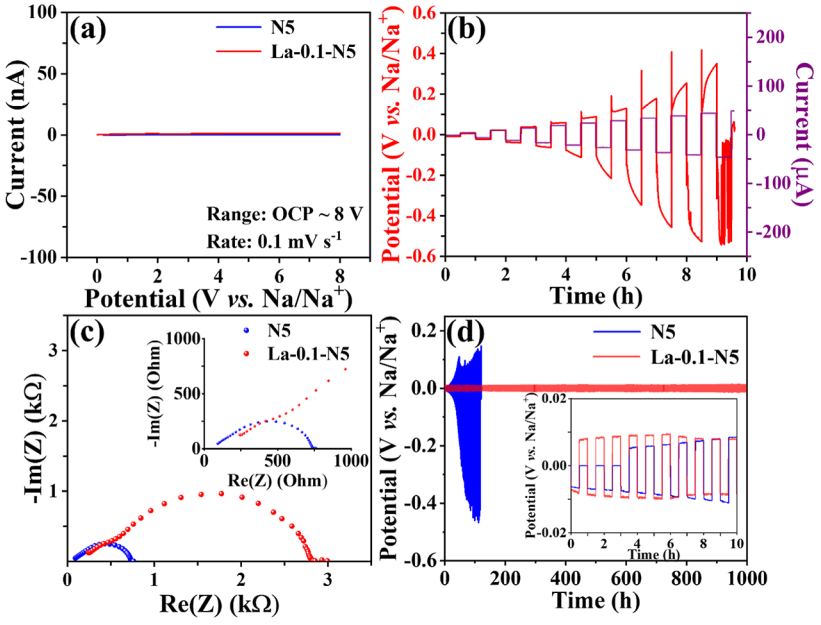

Figure 6. (a) LSV of $Na_5YSi_4O_{12}$ and $Na_5La_{0.1}Y_{0.9}Si_4O_{12}$, (b) DC cycling with stepwise increasing current of La-0.1-N5, (c) impedance spectra of N5 and La-0.1-N5 against sodium metal in symmetry cell, and (d) voltage development in a DC cycling experiment of N5 and La-0.1-N5 with 15 μA cm^{-2}.

https://doi.org/10.1021/acsaem.5c01301
ACS Appl. Energy Mater. 2025, 8, 9656−9662

polarization of N5 exceeded La-0.1-N5 after 8 h. La-0.1-N5 maintained a stable and flat voltage profile over the entire duration, reflecting a superior cycling stability. This performance enhancement could be attributed to improved grain boundary conductivity in La-0.1-N5, leading to effective sodium-ion migration and uniform sodium flux. In contrast, N5 exhibited short circuit due to the dendrite growth by uneven ion transport. Therefore, it is concluded that La doping to $Na_5YSi_4O_{12}$ reduces grain boundary resistance, enhancing sodium ion transport and suppressing the dendrite formation, which makes La-doped $Na_5YSi_4O_{12}$ a promising ceramic electrolyte for all-solid-state Na batteries.

4. CONCLUSIONS

Lanthanum was successfully doped into the $Na_5YSi_4O_{12}$ (N5) Na-ion conductor via a solid-state reaction. EDX and XRD analysis confirmed the successful incorporation of lanthanum into the N5 structure, with purity retained only at a lower doping level (x = 0.1). Higher doping ratios resulted in the formation of secondary phases and impurities. La-doping influenced the grain boundary conductivity, leading to a 3.3 times higher grain boundary conductivity for $Na_5La_{0.1}Y_{0.9}Si_4O_{12}$ compared to that of pristine N5. While La doping caused an expansion of lattice parameters, it did not significantly affect bulk conductivity, activation energy, and electronic conductivity. The electrochemical stability window of La-doped N5 remained unchanged, maintaining stability up to 8 V vs Na/Na^+. Additionally, the cycling performance of La-doped N5 for Na plating and stripping was significantly improved compared with pristine N5. The La-doped N5 is a promising electrolyte for all-solid-state Na batteries.

■ ASSOCIATED CONTENT

Supporting Information

The Supporting Information is available free of charge at https://pubs.acs.org/doi/10.1021/acsaem.5c01301.

Identification of impurities in $Na_5La_{0.4}Y_{0.6}Si_4O_{12}$, SEM analysis of La-doped N5, elemental distribution and atomic percentages of N5 and La-0.1-N5, electrochemical performance comparison, and detailed lattice parameters with site occupancy data (PDF)

■ AUTHOR INFORMATION

Corresponding Authors

Hailin Shen − *School of Chemical Engineering and Materials, Changzhou Institute of Technology, Changzhou 213028, China*; Email: shenhailin@czu.cn

Zhenghui Pan − *School of Materials Science and Engineering, Tongji University, Shanghai 201804, China*; orcid.org/0000-0002-4589-7072; Email: zhenghuipan@tongji.edu.cn

Masashi Kotobuki − *Battery Research Center of Green Energy, Ming Chi University of Technology, New Taipei City 24301, Taiwan; Center for Sustainability and Energy Technologies, Chang Gung University, Taoyuan City 33302, Taiwan*; orcid.org/0000-0001-7335-3833; Email: kotobuki@mail.mcut.edu.tw

Authors

Mohamed M. Abdelaal − *Battery Research Center of Green Energy, Ming Chi University of Technology, New Taipei City 24301, Taiwan; Tabbin Institute for Metallurgical Studies (TIMS), Cairo 11421, Egypt*; orcid.org/0000-0003-0452-7750

Zhongting Wang − *National Engineering Research Center for Magnesium Alloys, College of Materials Science and Engineering, Chongqing University, Chongqing 400044, China*

Complete contact information is available at: https://pubs.acs.org/10.1021/acsaem.5c01301

Notes

The authors declare no competing financial interest.

■ ACKNOWLEDGMENTS

This research was funded by the National Science and Technology Council of Taiwan (grant number: 111-2221-E-131-024-MY3, 112-2221-E-131-005-MY3, 114-2923-E-131-002-MY3), the Industry-Academic cooperation project (Project title: MCUT and Formosa Smart Energy Tech. Corp., Project number: I0-113-S028), and Chang Gung University (URRPD2N0021).

■ REFERENCES

(1) Liao, W.-L.; Hung, T.-F.; Abdelaal, M. M.; Chao, C.-H.; Fang, C.-C.; Mohamed, S. G.; Yang, C.-C. Highly efficient sodium-ion capacitor enabled by mesoporous $NaTi_2(PO_4)_3$/C anode and hydrogel-derived hierarchical porous activated carbon cathode. *J. Energy Storage* **2022**, *55*, 105719.

(2) Liao, W.-L.; Abdelaal, M. M.; Amirtha, R.-M.; Fang, C.-C.; Yang, C.-C.; Hung, T.-F. In Situ Construction of Nitrogen-Doped and Zinc-Confined Microporous Carbon Enabling Efficient Na^+-Storage Abilities. *Int. J. Mol. Sci.* **2023**, *24* (10), 8777.

(3) Abdelaal, M. M.; Yang, C.-C.; Hung, T.-F. Electrochemical performances and Li^+-storage mechanism of highly proportional 1T-MoS_2/hierarchical porous activated carbon nanocomposites. *J. Energy Storage* **2024**, *77*, 109926.

(4) Hou, J.; Xu, T.; Wang, B.; Yang, H.; Wang, H.; Kong, D. Z.; Lyu, L.; Li, X.; Wang, Y.; Xu, Z. L. Self-Confinement of Na Metal Deposition in Hollow Carbon Tube Arrays for Ultrastable and High-Power Sodium Metal Batteries. *Adv. Funct. Mater.* **2024**, *34*, 2312750.

(5) Hüttl, J.; Cai, W.; Wagner, D.; Schilm, J.; Kusnezoff, M.; Nikolowski, K.; Shaji, N.; Lee, C. W.; Partsch, M.; Michaelis, A. Polarization impedance at the Na-$Na_5YSi_4O_{12}$ interface. *Solid State Ionics* **2022**, *376*, 115856.

(6) Yan, B.; Wang, Z.; Ren, H.; Lu, X.; Qu, Y.; Liu, W.; Jiang, K.; Kotobuki, M. Interfacial modification of $Na_3Zr_2Si_2PO_{12}$ solid electrolyte by femtosecond laser etching. *Ionics* **2023**, *29* (2), 865−870.

(7) Amirtha, R. M.; Chang, S.-M.; Abdelaal, M. M.; Yang, C.-C.; Hung, T.-F. Efficient zinc protection enabled by polyhedral metal-organic framework and ionic-crosslinking binder. *Electrochim. Acta* **2024**, *496*, 144526.

(8) Gunamony, J.; Walle, K. Z.; Kotobuki, M. Influence of mixing technique on properties of $Li_{1.3}Al_{0.3}Ti_{1.7}(PO_4)_3$ solid electrolyte prepared by the solid-state reaction-A comparison of dry 3D mixing technique with wet ball-milling. *Solid State Ionics* **2024**, *410*, 116528.

(9) Tietz, F. Sodium-ion-conducting Oxides Used as Solid Electrolytes in Sodium Batteries − Learning from the Past. In *Sodium-Ion Batteries*, Wiley Online Library, 2022; pp 391−428.

(10) Okura, T.; Yamashita, K. New Na^+ Superionic Conductor Narpsio Glass-Ceramics. In *Theoretical Chemistry for Advanced Nanomaterials: Functional Analysis by Computation and Experiment*; Onishi, T., Ed.; Springer: Singapore, 2020; pp 383−416.

(11) Többens, D. M.; Kahlenberg, V.; Kaindl, R.; Sartory, B.; Konzett, J. $Na_{8.25}Y_{1.25}Si_6O_{18}$ and its family of zwölfer ring silicates. *Z. Kristallogr. - Cryst. Mater* **2008**, *223* (6), 389−398.

(12) Okura, T.; Kawada, K.; Yamashita, K. Microstructural effects on sodium ion conduction properties of grains and grain boundaries of $Na_5YSi_4O_{12}$-type silicophosphate glass-ceramics. *J. Ceram. Soc. Jpn.* **2022**, *130* (1), 10−15.
(13) Sun, G.; Yang, X.; Chen, N.; Yao, S.; Wang, X.; Jin, X.; Chen, G.; Xie, Y.; Du, F. $Na_5YSi_4O_{12}$: A sodium superionic conductor for ultrastable quasi-solid-state sodium-ion batteries. *Energy Storage Mater.* **2021**, *41*, 196−202.
(14) Li, Y.; Sun, Z.; Yuan, X.; Jin, H.; Zhao, Y. NaBr-Assisted Sintering of $Na_3Zr_2Si_2PO_{12}$ Ceramic Electrolyte Stabilizes a Rechargeable Solid-state Sodium Metal Battery. *ACS Appl. Mater. Interfaces* **2023**, *15* (42), 49321−49328.
(15) Lei, J.; Liu, Z.; Zou, F.; Wang, B.; Liao, R.; Dmytro, S.; Zhang, Q. La_2O_3 optimized the structure and ionic conductivity of $0.75Li_2O$-$0.125B_2O_3$-$0.125SiO_2$ ceramic solid electrolyte sintering additives. *Ionics* **2023**, *29* (9), 3549−3557.
(16) Kindelmann, M.; Escolastico, S.; Almar, L.; Vayyala, A.; Jennings, D.; Deibert, W.; Meulenberg, W. A.; Rheinheimer, W.; Bram, M.; Serra, J. M.; et al. Highly conductive grain boundaries in cold-sintered barium zirconate-based proton conductors. *J. Mater. Chem. A* **2024**, *12* (7), 3977−3988.
(17) Qian, C.; Hu, K.; Shen, Z.; Wang, Q.; Li, P.; Lu, Z. Effect of sintering aids on mechanical properties and microstructure of alumina ceramic via stereolithography. *Ceram. Int.* **2023**, *49* (11), 17506−17523.
(18) Hoinkis, N.; Schuhmacher, J. r.; Fuchs, T.; Leukel, S.; Loho, C.; Roters, A.; Richter, F. H.; Janek, J. r. Amorphous Phase Induced Lithium Dendrite Suppression in Glass-Ceramic Garnet-Type Solid Electrolytes. *ACS Appl. Mater. Interfaces* **2023**, *15* (23), 28692−28704.
(19) Ding, Y.; Liu, H.; Xue, H.; Cong, P.; Zhao, Y.; Xiang, B.; Xia, C. Improving the green mechanical strength and thermal shock resistance of colloidal silica-bonded castables using La_2O_3. *Int. J. Appl. Ceram. Technol.* **2024**, *21* (1), 476−484.
(20) Shweta; Avinashi, S. K.; Hussain, A.; Fatima, Z.; Sharma, K.; Khanka, S.; Prakash, R.; Singh, D.; Gautam, C. Structural, morphological and mechanical insights from La_2O_3 doped machinable silicate glass ceramics for biomedical applications. *Ceram. Int.* **2023**, *49* (6), 8801−8819.
(21) Kamran, M.; Abbas, Y.; Anis-ur-Rehman, M. Effect of Ce^{3+} and La^{3+} co-substitution on transport properties of spinel Co-Ferrites. *Inorg. Chem. Commun.* **2023**, *155*, 111034.
(22) Zhou, T.; Chen, Y. Heterojunction of Y^{3+}-substituted $Na_3V_2(PO_4)_3$-$NaYO_2$ accelerating kinetics with superior performance for full sodium-ion batteries. *J. Colloid Interface Sci.* **2024**, *654*, 1163−1176.
(23) Wang, Y.; Wang, Z.; Zheng, F.; Sun, J.; Oh, J. A. S.; Wu, T.; Chen, G.; Huang, Q.; Kotobuki, M.; Zeng, K.; Lu, L. Ferroelectric Engineered Electrode-Composite Polymer Electrolyte Interfaces for All-Solid-State Sodium Metal Battery. *Adv. Sci.* **2022**, *9* (13), 2105849.
(24) Abdelaal, M. M.; Mohamed, S.; Barakat, Y. F.; Derbala, H. A. Y.; Hassan, H. H.; Al Zoubi, W. N-Aminophthalimide as a Synthon for Heterocyclic Schiff bases: Efficient Utilization as Corrosion Inhibitors of Mild Steel in 0.5 $mol.L^{-1}$ H_2SO_4 Solution. *Egypt. J. Chem.* **2018**, *61* (3), 539−558.
(25) Ferrer-Nicomedes, S.; Mormeneo-Segarra, A.; Vicente-Agut, N.; Barba-Juan, A. Fine-tuning the microstructure for improved performance in cold-sintered $Li_{1.3}Al_{0.3}Ti_{1.7}(PO_4)_3$ composite solid electrolytes. *Ceram. Int.* **2024**, *50* (21), 44330−44338.
(26) Lee, R.-H.; Kang, C.-Y.; Lee, J.-K.; Jin, B.-S.; Kim, K.-N.; Kim, H.-S.; Yoon, J.-R.; Lee, S.-H. Tailoring the grain boundary structure and chemistry of the dendrite-free garnet solid electrolyte $Li_{6.1}Ga_{0.3}La_3Zr_2O_{12}$. *NPG Asia Mater.* **2024**, *16* (1), 42.
(27) Deivanayagam, R.; Shahbazian-Yassar, R. Electrochemical methods and protocols for characterization of ceramic and polymer electrolytes for rechargeable batteries. *Batter. Supercaps.* **2021**, *4* (4), 596−606.
(28) Gami, P.; Badole, M.; Vasavan, H. N.; Das, A. K.; Saxena, S.; Dagar, N.; Srihari, V.; Kumar, S. NASICON-type medium entropy $Li_{1.5}Sn_{1.0}Al_{0.5}Zr_{0.5}(PO_4)_3$ electrolyte for solid state Li metal batteries. *J. Power Sources* **2024**, *618*, 235214.
(29) Meng, W.; Han, W.; Dai, L.; Wang, L.; Tang, X.; Liu, S. Stable anode interface regulation of solid sodium battery through oxygen potential regulation. *Chem. Eng. J.* **2023**, *475*, 145984.
(30) Hernández-Palomares, A.; Espejel-Ayala, F. Precipitated silica, alkali silicates and zeolites from construction and demolition waste materials. *J. Cleaner Prod.* **2022**, *348*, 131346.
(31) Upadhyay, K.; Thomas, S.; Tamrakar, R. K.; Kalarikkal, N.; Butoliya, S. Comparative study of structural and optical behavior of Er^{3+} doped Y_2SiO_5 phosphor prepared by different methods. *Mater. Sci. Eng., B* **2022**, *275*, 115511.
(32) Yang, A.; Ye, R.; Li, X.; Lu, Q.; Song, H.; Grüner, D.; Ma, Q.; Tietz, F.; Fattakhova-Rohlfing, D.; Guillon, O. Fabrication of thin sheets of the sodium superionic conductor $Na_5YSi_4O_{12}$ with tape casting. *Chem. Eng. J.* **2022**, *435*, 134774.
(33) Yang, M.; Zhuang, Y.; Xing, P. High-performance B_4C-LaB_6 composite ceramics fabricated via hot-pressing sintering with La_2O_3 as sintering additive. *Ceram. Int.* **2021**, *47* (23), 32675−32684.
(34) Zan, W.; Ma, B.; Tang, J.; Liu, K.; Cao, Y.; Tian, J.; Jiang, Z. Preparation and properties of $MgAl_2O_4$ spinel ceramics by double-doped CeO_2 and La_2O_3. *Ceram. Int.* **2023**, *49* (10), 15164−15175.
(35) Liu, L.; Xu, Y.; Zhou, X.; Guo, W.; Li, J.; Guo, X.; Jiang, Y. Conductivity behavior of $Na_5YSi_4O_{12}$ and its typical structural analogues by solution-assisted solid-state reaction for solid-state sodium battery. *J. Solid State Chem.* **2024**, *336*, 124781.
(36) Abdelaal, M. M.; Hung, T.-C.; Mohamed, S. G.; Yang, C.-C.; Hung, T.-F. Two Birds with One Stone: Hydrogel-Derived Hierarchical Porous Activated Carbon toward the Capacitive Performance for Symmetric Supercapacitors and Lithium-Ion Capacitors. *ACS Sustainable Chem. Eng.* **2022**, *10* (14), 4717−4727.
(37) Abdelaal, M. M.; Hung, T.-C.; Mohamed, S. G.; Yang, C.-C.; Huang, H.-P.; Hung, T.-F. A Comparative Study of the Influence of Nitrogen Content and Structural Characteristics of NiS/Nitrogen-Doped Carbon Nanocomposites on Capacitive Performances in Alkaline Medium. *Nanomaterials* **2021**, *11* (7), 1867.
(38) Sau, K.; Takagi, S.; Ikeshoji, T.; Kisu, K.; Sato, R.; dos Santos, E. C.; Li, H.; Mohtadi, R.; Orimo, S.-i. Unlocking the secrets of ideal fast ion conductors for all-solid-state batteries. *Communications Materials* **2024**, *5* (1), 122.
(39) Chen, C.; Sun, Y.; He, L.; Kotobuki, M.; Hanc, E.; Chen, Y.; Zeng, K.; Lu, L. Microstructural and Electrochemical Properties of Al- and Ga-Doped $Li_7La_3Zr_2O_{12}$ Garnet Solid Electrolytes. *ACS Appl. Energy Mater.* **2020**, *3* (5), 4708−4719.
(40) Yang, A.; Yao, K.; Schaller, M.; Dashjav, E.; Li, H.; Zhao, S.; Zhang, Q.; Etter, M.; Shen, X.; Song, H.; Lu, Q.; Ye, R.; Moudrakovski, I.; Pang, Q.; Indris, S.; Wang, X.; Ma, Q.; Tietz, F.; Chen, J.; Guillon, O. Enhanced room-temperature Na^+ ionic conductivity in $Na_{4.92}Y_{0.92}Zr_{0.08}Si_4O_{12}$. *eScience* **2023**, *3* (6), 100175.
(41) Abdelaal, M. M.; Hsu, H.-H.; Liao, W.-L.; Mohamed, S. G.; Yang, C.-C.; Hung, T.-F. Hierarchical porous activated carbon anode for dual carbon lithium-ion capacitors: Energy storage mechanisms and electrochemical performances. *J. Taiwan Inst. Chem. Eng.* **2024**, *154*, 104912.

https://doi.org/10.1021/acsaem.5c01301
ACS Appl. Energy Mater. 2025, 8, 9656−9662